Correspondence to:
Y. Yu,
yuyouqiang@tongji.edu.cn

Topography of the 410 and 660 km Discontinuities Beneath the Cenozoic Okavango Rift Zone and Adjacent Precambrian Provinces

Youqiang Yu[1] [iD], **Stephen S. Gao[2]** [iD], and **Kelly H. Liu[2]** [iD]

[1]State Key Laboratory of Marine Geology, Tongji University, Shanghai, China, [2]Geology and Geophysics Program, Missouri University of Science and Technology, Rolla, MO, USA

Abstract By taking advantage of the recent availability of a broadband seismic data set from Networks NR and BX covering the entire country of Botswana, we conduct a systematic receiver function investigation of the topography of the 410 and 660 km discontinuities beneath the incipient Okavango rift zone (ORZ) in northern Botswana and its adjacent Archean-Proterozoic tectonic provinces in southern Africa. Similar to a previous mantle transition zone (MTZ) discontinuity study using data from a 1-D profile traversing the ORZ, a normal MTZ thickness is observed in most parts of the study area. This is inconsistent with the existence of widespread positive thermal anomalies in the MTZ and further implies that active thermal upwelling from the lower mantle plays an insignificant role in the initiation of continental rifting. The results also suggest that cold temperature presumably associated with thick cratonic keels has indiscernible influence on the thermal structure of the MTZ. The expanded data set reveals several isolated areas of slight (~10 km or smaller) MTZ thinning. The largest of such areas has a NE-SW elongated shape and is mostly caused by relative deepening of the 410 km discontinuity rather than shallowing of the 660 km discontinuity. These characteristics are different from those expected for a typical mantle plume. We speculate that the thinner-than-normal MTZ may be induced by minor thermal upwelling associated with late Mesozoic-early Cenozoic lithospheric delamination, a recently proposed mechanism that might be responsible for the high elevation of southern Africa.

1. Introduction

Continental rifting plays an essential role in the evolution of continental lithosphere. Whether the initiation of continental breakup is linked to thermal anomalies originating from the lower mantle in the form of mantle plumes or by other processes remains controversial (e.g., King & Anderson, 1998; Korenaga, 2004; Rychert et al., 2012; Sengör & Burke, 1978). Situated at the southernmost terminus of the southwestern branch of the East African Rift System (EARS), the Okavango rift zone (ORZ) is one of the youngest continental rifts, with an estimated time of initiation between 120 and 40 ka (Modisi et al., 2000; Reeves, 1972). It is thus an ideal location to explore tectonic processes associated with the incipient-stage development of continental rifting and its relationship with deep mantle dynamics.

The ORZ develops in the Damara Belt and Rehoboth Province, which are the major components of a system of dominantly NE-SW trending Proterozoic mobile belts situated between the Archean Congo Craton to the northwest and the Kaapvaal and Zimbabwe cratons to the southeast (Figure 1). The Kaapvaal (formed and stabilized between 3.6 and 2.6 Ga) and Zimbabwe (3.5 to 2.6 Ga) cratons collided at about 2.7–2.6 Ga and formed the Limpopo Belt (Begg et al., 2009; de Wit et al., 1992), creating the Kalahari Craton. Similar to other areas in southern Africa, the study area (Figure 1) shows an anomalously high elevation for pre-Cambrian terranes, with a mean value of 1,034 m above sea level. A large low shear velocity province (LLSVP) in the lower mantle is imaged beneath southern Africa (Ritsema et al., 2011) and is proposed to be responsible for the high elevation (e.g., Fishwick & Bastow, 2011; Gurnis et al., 2000; Lithgow-Bertelloni & Silver, 1998; Ritsema et al., 2011). Mantle plumes originating from the African LLSVP have been proposed to tilt northward and further promote the initiation and development of the currently mature segments of the EARS (e.g., Hansen et al., 2012; Mulibo & Nyblade, 2013), although such a mechanism remains debated (e.g., Reed et al., 2016; Rychert et al., 2012; Stamps et al., 2015). Given the fact that the ORZ directly situates above the LLSVP, a reliable assessment on the question of whether thermal upwelling possibly associated with the
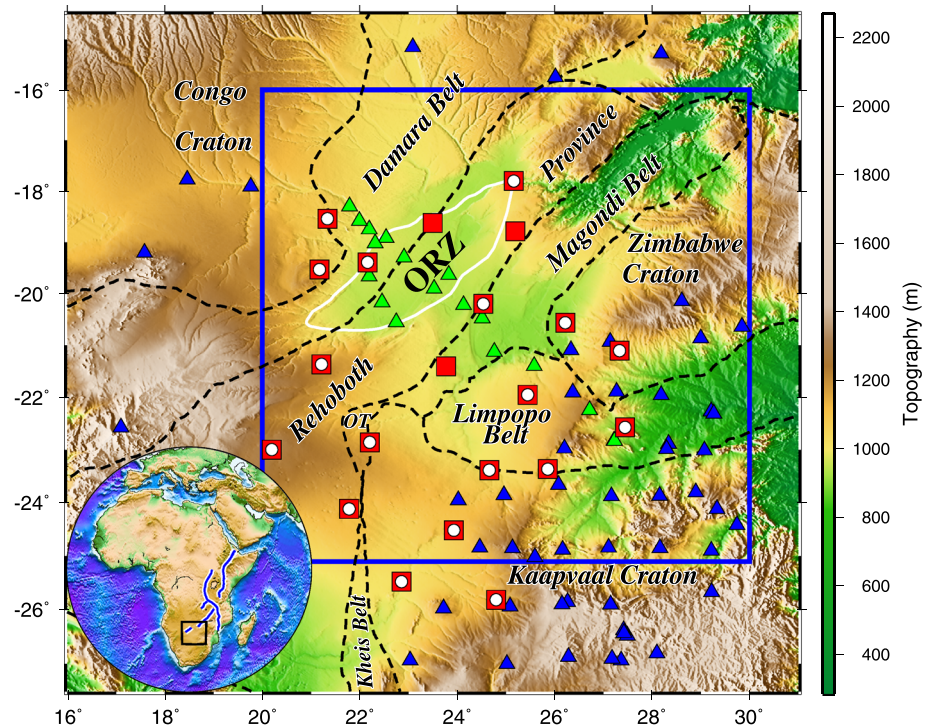
Figure 1. Topographic map of the study area showing major tectonic setting and seismic stations used in this study. The blue rectangle shows the study area. Black dashed lines delineate the tectonic boundaries modified from Hanson (2003). Red squares and white dots indicate new seismic stations from the Botswana Network of Autonomously Recording Seismographs (21 stations, Fadel et al., 2018) and the Botswana Seismological Network (18 stations), respectively. Green triangles are the 17 SAFARI stations used in Yu, Liu, Moidaki, et al. (2015). The other stations are plotted as blue triangles mainly belonging to seismic networks of AF and XA. ORZ = Okavango rift zone; OT = Okwa Terrane. The white lines depict the ORZ. The inset displays the location of the study area, which is indicated by the black rectangle, and the blue lines denote the rift axes of the East African Rift System.

LLSVP has reached the upper mantle or remains in the lower mantle is important for understanding the mechanisms for the initiation and early stage development of the ORZ and other continental rifts. Previous studies have demonstrated that one of the most effective approaches to address this question is to map the topography and investigate associated thermal anomalies of the mantle transition zone (MTZ), a layer between the 410 km (d410) and 660 km (d660) discontinuities.

The d410 and d660 represent mineralogical phase transitions of olivine-wadsleyite and ringwoodite-bridgmanite, respectively (Ringwood, 1975). Lateral variations of their depths offer present-day thermal state of the MTZ (Ringwood, 1975). Experimental studies indicate that the d410 and d660 have positive and negative Clapeyron slopes in an olivine-dominated phase-transition system, respectively (Bina & Helffrich, 1994). Consequently, a positive thermal anomaly associated with a mantle upwelling penetrating the MTZ would induce depression of the d410 and uplift of the d660, leading to thinning of the MTZ. Similarly, the presence of negative temperature anomalies such as those associated with cold subducting slabs or lithospheric dripping corresponds to MTZ thickening. Compositional variations such as water content may also influence the MTZ structure. In particular, the presence of hydrous minerals plays a similar role as low temperature, that is, shifting the d410 and d660 to lower and higher pressures, respectively, and thickening the MTZ (Litasov et al., 2005). Under high-temperature (beyond 1800°C) conditions, the phase transition at the d660 would be characterized as possessing a positive Clapeyron slope and dominated by the transition from majorite garnet to perovskite (Hirose, 2002).

The vast majority of seismological studies on the upper mantle and MTZ structure beneath the ORZ and its adjacent areas mostly rely on broadband seismic data recorded by two groups of stations (Figure 1): the Southern Africa Seismic Experiment (SASE, James et al., 2001) covering the Kaapvaal and Zimbabwe cratons and a NW-SE profile across the ORZ as part of the Seismic Arrays for African Rift Initiation

(SAFARI, Gao et al., 2013). Beneath the study area, most previous receiver function (RF) investigations targeting the cratonic areas find an MTZ thickness that is generally comparable to the global average of 250 km (e.g., Gao et al., 2002; Julià & Nyblade, 2013; Niu et al., 2004; Sun et al., 2018), suggesting the lack of observable influence of the lower mantle African LLSVP and the cold cratonic root on the thermal structure of the MTZ. A study using the 17-station SAFARI data by Yu, Liu, Moidaki, et al. (2015) suggests an overwhelmingly normal MTZ thickness in the vicinity of the ORZ. This observation, together with results from other studies using the SAFARI data, including minor ($\leq$ ~5 km) crustal thinning (Fadel et al., 2018; Yu, Liu, Reed, et al., 2015), absence of rifting-related mantle flow field as revealed by shear wave splitting analysis (Yu, Gao, et al., 2015), and small (~ −1%) velocity anomalies in the upper mantle directly beneath the rift zone compared to other continental rifts (Yu et al., 2017), is inconsistent with the hypothesis that active mantle upwelling plays a major role in rift initiation. Minor mantle velocity anomalies associated with the ORZ are also suggested by recent body (Ortiz et al., 2019) and surface wave (Fadel et al., 2020) seismic tomography studies utilizing the same data set that is used for MTZ discontinuity imaging in this study.

Based on the SAFARI data alone, a thinner-than-normal MTZ with a maximum amount of ~10 km thinning is revealed in an apparently circular area with a radius of ~100 km beneath central-west Botswana adjacent to the south side of the ORZ, along the edge of the area sampled by the linear profile where the ray coverage is limited (Yu, Liu, Moidaki, et al., 2015). The existence and the spatial extent of this potentially interesting feature could not be examined due to the limited station coverage. In addition, the limited spatial coverage by the SAFARI stations could not confidently exclude the possibility that lower mantle thermal upwelling enters the MTZ and upper mantle beneath areas outside the covered area and travels horizontally to the ORZ. A recent body wave tomography reveals a craton-like root beneath southern Rehoboth Province (Ortiz et al., 2019), and whether such a thick lithosphere affects the MTZ is unknown. In this study, we take full advantage of the recent availability of a broadband seismic data set recorded by 39 stations under seismic networks of BX and NR (Figure 1; Fadel et al., 2018, 2020) to conduct a systematic investigation of MTZ structure beneath the ORZ and its surrounding regions. The greatly expanded data set enables us to image the MTZ discontinuities beneath a much larger area with a higher spatial resolution.

2. Data and Methods

2.1. Data

All the three-component broadband teleseismic data used in this study are publicly available and were requested from the Incorporated Research Institutions for Seismology (IRIS) Data Management Center (DMC) recorded over the period between mid-1993 and early 2019 by a total of 111 stations. When stations that are 1 km or closer from each other are combined, the stations occupy about 92 different sites in an area that is slightly larger than the study area (Figure 1). Depending on the arriving azimuth, some of the seismic rays received by stations outside the study area traverse one or both MTZ discontinuities in the study area; therefore, adding data from stations outside the study area can improve ray coverage on the edges of the area. The data set was mainly from the following networks: (1) NR (10.7914/SN/NR): the Botswana Network of Autonomously Recording Seismographs (BNARS; 21 stations, operated between November 2013 and August 2016, Fadel et al., 2018), (2) BX: the Botswana Seismological Network (BSN; 18 stations, operated since February 2018). Most seismic stations in the above two networks are colocated with each other (Figure 1) and approximately evenly cover the whole country of Botswana. (3) XA (10.7914/SN/XA_1997): SASE (39 stations, operated between 1997 and 1999, James et al., 2001), and (4) XK (10.7914/SN/XK_2012): SAFARI (17 stations, operated between May 2012 and August 2014, Gao et al., 2013; Yu, Liu, Moidaki, et al., 2015). Earthquakes used in the study have an epicentral distance in the range of 30–100°, and their cutoff magnitudes are determined by employing an empirical formula taking both the epicentral distance and the focal depth into consideration, for the purpose of balancing the quantity and quality of the requested data (Liu & Gao, 2010).

The data processing procedure and parameters are identical to those employed by Gao and Liu (2014b) for imaging the d410 and d660 beneath the contiguous United States and are briefly summarized here. The selected seismograms are windowed 20 s before and 260 s after the first compressional wave predicted from the IASP91 Earth model (Kennett & Engdahl, 1991) and then band-pass filtered by a four-pole two-pass
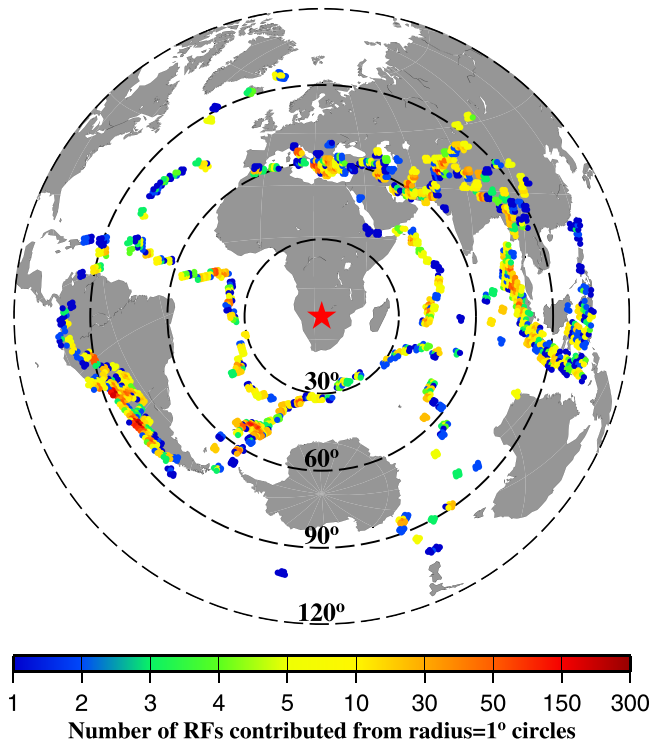
Figure 2. Azimuthal equidistant projection map showing the spatial distribution of earthquakes. Each dot indicates events in a radius = 1° circular area, and its color represents the number of RFs contributed from this circle. Red star shows the center of the study region, and the concentric black dashed circles indicate distance in degree from the center of the study area.

Bessel filter in the frequency band of 0.02–0.2 Hz. The frequency domain deconvolution procedure (Ammon, 1991) with a water level of 0.03 is employed to generate the radial RFs by deconvolving the vertical from the radial components of those three-component seismograms with signal-to-noise ratios (SNRs) exceeding 4 on the radial component. A set of exponential functions are adopted to minimize the degenerating effects of the strong *PP* phase in a 60 s window centered at the theoretical *PP* arrivals. The resulting RFs are subsequently subjected to an SNR-based procedure to further remove those low-quality RFs without a clear first *P* arrival or with strong noise. As a result, we obtain a total of 6,215 high-quality RFs from 1,234 events (Figure 2) among which 1,817 RFs are from the 39 stations in Botswana that have not been used in previous MTZ investigations (Figure 1).

2.2. RF Stacking

We employ the approach of Gao and Liu (2014a) to conduct moveout correction and stacking of the RFs. The approach utilizes a non-plane wave assumption, which takes the difference of the ray parameters between the direct *P* and the *P*-to-*S* converted phases into account. The location of the ray piercing points for each of the high-quality RFs is calculated at the middle of the MTZ (535 km) based on the IASP91 Earth model, and all the RFs are grouped into circular bins with a radius of 1° based on the location of the piercing points (Figure 3). The distance between the centers of neighboring bins is 1 geographic degree. RFs in each of the bins are moveout corrected and stacked to generate depth series in the depth range of 300–800 km with a vertical interval of 1 km. The arrivals of the d410 and d660 are first picked by automatically searching for the maximum stacking amplitude in the depth range of 380–440 km for the d410 and 630–690 km for the d660, and the searching ranges for a few bins are manually adjusted to make the resulting depths consistent with neighboring bins. Bins with less than 20 RFs are not used, and all the stacked traces in the remaining bins are visually verified to reject ambiguous arrivals with either multiple similar-amplitude or weak peaks corresponding to the MTZ discontinuities. A bootstrap approach with 50 resampling iterations (Efron & Tibshirani, 1986) is applied to quantify the average MTZ discontinuity depths and their associated uncertainties for each bin (Figure S1 in the supporting information).

2.3. Estimation of Lithospheric Thickness From the Apparent Depth of the d410

The resulting MTZ discontinuity depths are apparent rather than true depths due to the employment of the one-dimensional IASP91 standard Earth model for moveout correction and time-depth conversion. For each of the bins, the apparent depth (D_A) of a given discontinuity (d410 or d660) can be converted into true depth (D_T) using (Equation 8 in Gao & Liu, 2014a):

$$D_T = \frac{(V_{S0} + \delta V_S) \times (V_{P0} + \delta V_P)}{(V_{P0} + \delta V_P) - (V_{S0} + \delta V_S)} \times \frac{V_{P0} - V_{S0}}{V_{P0} \times V_{S0}} D_A \tag{1}$$

where V_{P0} and V_{S0} are the mean *P* (V_P) and *S* (V_S) velocities in the Earth model from the surface to the discontinuity and δV_P and δV_S are mean velocity anomalies (in km/s) from the surface to the discontinuity. Clearly, reliable true depths can only be obtained when reliably determined V_P and V_S anomalies are available from the surface to the bottom of the MTZ. Additionally, the velocity anomalies need to be the absolute difference between the true and reference velocities in the Earth model, rather than relative to the mean velocities in a layer. The latter is a common practice in seismic body wave tomography studies, especially for those conducted in a regional scale (Foulger et al., 2013). Unfortunately, such velocity models are nonexistent for the study area. If low-resolution global-scale velocity models are used for correction, possible errors in the models can lead to misleading conclusions, as systematically demonstrated in Mohamed et al. (2014). For comparison, a regional (Youssof et al., 2015) and a global (Lu et al., 2019)
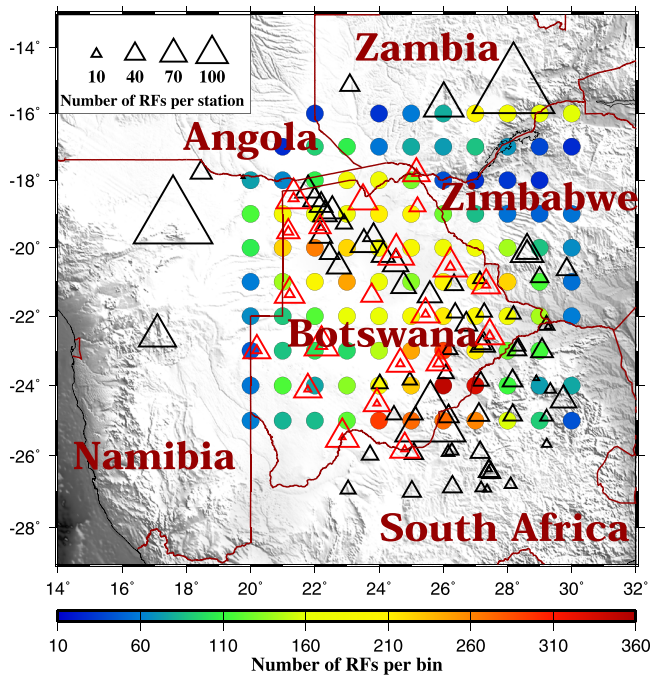
Figure 3. Distribution of the center of circular bins (dots) for grouping RFs and seismic stations (triangles) used in the study. The size of the triangles and the color of the circles indicate the number of RFs at each station and within each bin, respectively. Red triangles highlight the new stations from NR and BX networks.

tomography model (including both V_P and V_S) are employed to correct the apparent depths based on Equation 1.

Under the assumptions that (1) the true depth of the d410 is 410 km and (2) lateral variations of upper mantle mean velocities are solely related to changes in lithospheric thickness, the observed apparent depth of the d410 can be used to estimate the thickness of the lithosphere (Sun et al., 2018). Under the above assumptions, we can obtain δV_P of each bin using Equation 1 by incorporating the apparent depth of the d410 and a γ factor, which is defined as $dln(V_S)/dln(V_P)$. For this study, a γ of 1.7, which is the same as the value found for the tectonically stable central and eastern United States (Gao & Liu, 2014b), is used. The lithospheric thickness (H_{LAB}) beneath a circular bin can be estimated using the following equation derived from Equation 1 (Sun et al., 2018):

$$\frac{H_{LAB} - H_{REF}}{\delta V_P} = \frac{410}{V_{LAB}} + H_{REF} \qquad (2)$$

where H_{REF} represents the lithospheric thickness at a reference location and is assigned a value of 90 km (Rychert & Shearer, 2009) and V_{LAB} denotes the V_P contrast between the lithosphere and the asthenosphere (in percent) which is given a value of 4% (Rychert & Shearer, 2009). Note that applications of different γ, H_{REF}, and V_{LAB} values would influence the magnitude of H_{LAB}, but not the pattern of its spatial variations. For an apparent d410 depth of 405 km, an increase of γ, H_{REF}, and V_{LAB} by 10% would lead to a -6.4, $+9.0$, and -4.5 km change of the estimated lithospheric thickness, respectively.

3. Results

All the resulting depth series with clearly identifiable MTZ discontinuity arrivals are plotted along the 10 latitudinal profiles in Figure 4. Almost all the d410 and d660 arrivals display high SNR and can be unambiguously identified. The robustness of the arrivals becomes more evident when the resulting depth series are plotted according to the apparent depths of the discontinuities (Figure 5). A total of 104 bins possesses prominent peaks of either the d410 or the d660, among which 102 and 96 bins demonstrate reliable d410 and d660 arrivals, respectively, and both discontinuities are observed in 94 bins (Figure 6). The number of RFs inside each bin ranges from 27 to 348 with a mean of 134 ± 75 (Figures 3 and 5). In the following, we assume that the MTZ is mainly associated with olivine-dominated phase transitions, which possibly prevail in the study area.

The cross-correlation coefficient (XCC) between the velocity-corrected d410 and d660 depths can be employed to evaluate the accuracy of the wave speed corrections (Gao & Liu, 2014b). Velocity anomalies above the d410 would induce positive correlations between the apparent depths of the d410 and d660. In contrary, the existence of water or thermal anomalies in the MTZ would lead to negative correlations between the corrected depths of the d410 and d660. Therefore, the resulting XCC after velocity correction should theoretically reduce to zero or become a negative value under the absence and existence of thermal/water content anomalies in the MTZ, respectively. The XCC between the resulting apparent depths of the d410 and d660 is 0.7 (Figure 7), and there is no reduction of the XCC between the corrected depths (Figure S2) when a regional model of Youssof et al. (2015) is used for wave speed correction. A reduction of the XCC from 0.7 to 0.54 is obtained by employing the global model of Lu et al. (2019), although the corrected depths of the d410 and d660 are still positively correlated (Figure S3), suggesting that the correction is inadequate. Thus, the following discussions will mostly rely on the apparent depths. It is worth to mention that the change of the MTZ thickness, based on which the main conclusions are drawn, is almost identical before and after the corrections (Figures 6c, S2c, and S3c) for the vast majority of the bins.
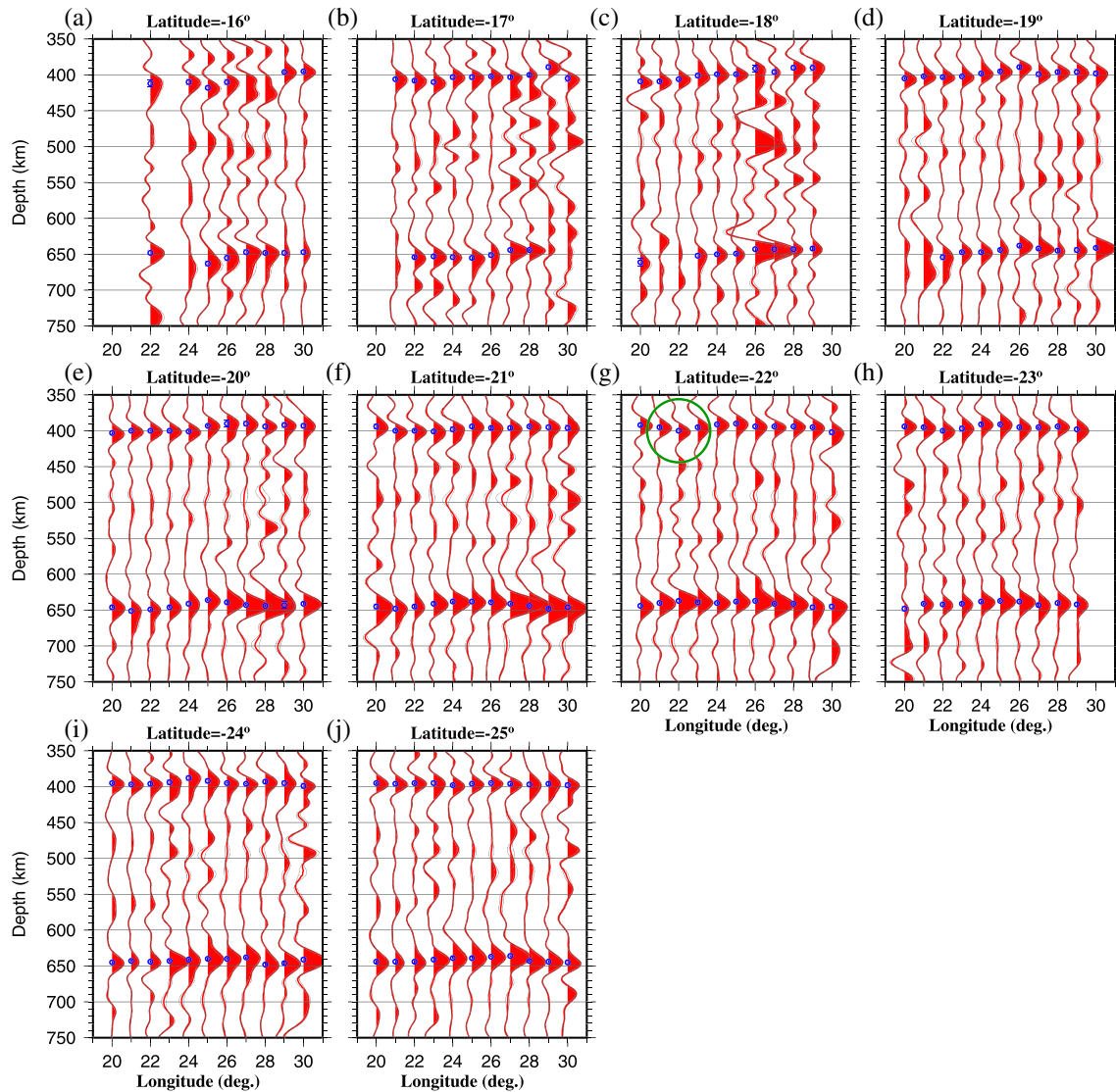
Figure 4. (a–j) Depth series from stacking moveout-corrected RFs within each bin plotted along 10 latitudinal profiles. The traces indicate the averaged depth series from all the 50 bootstrap iterations, and the blue circles with error bars represent the determined apparent depths of the MTZ discontinuities. The green circle in (g) highlights the relative deepening of the d410.

3.1. Discontinuity Topography and MTZ Thickness

The resulting apparent depths of the d410 and d660 for the entire study area (Figure 6) display a first-order parallelism highlighted by the positive XCC of 0.70 and averages of 398 ± 6 and 644 ± 5 km, respectively, which are significantly shallower than the values of 410 and 660 km in the IASP91 Earth model. The MTZ beneath the majority of the study area has a normal thickness with slight perturbations (less than 5 km). The average MTZ thickness is 247 ± 4 km, which is in agreement with recent RF observations (246 ± 7 km) in a larger area in southern Africa that did not use the BNARS and BSN data (Sun et al., 2018). Additionally, observations from this study are almost identical to the corresponding values of 398 ± 6, 646 ± 7, and 248 ± 6 km, respectively, obtained using the SAFARI data alone (Yu, Liu, Moidaki, et al., 2015).

Both the d410 and d660 beneath the Kalahari Craton are revealed to have a 15–20 km apparent uplift (395 ± 3 km for the former and 642 ± 3 km for the latter) with an average MTZ thickness of 246 ± 4 km, which is in agreement with most previous MTZ investigations in the area (Gao et al., 2002; Julià & Nyblade, 2013; Niu et al., 2004; Sun et al., 2018) but is inconsistent with the existence of a 20 km thicker-than-normal MTZ suggested by Blum and Shen (2004). The d410 and d660 beneath the ORZ (with depths
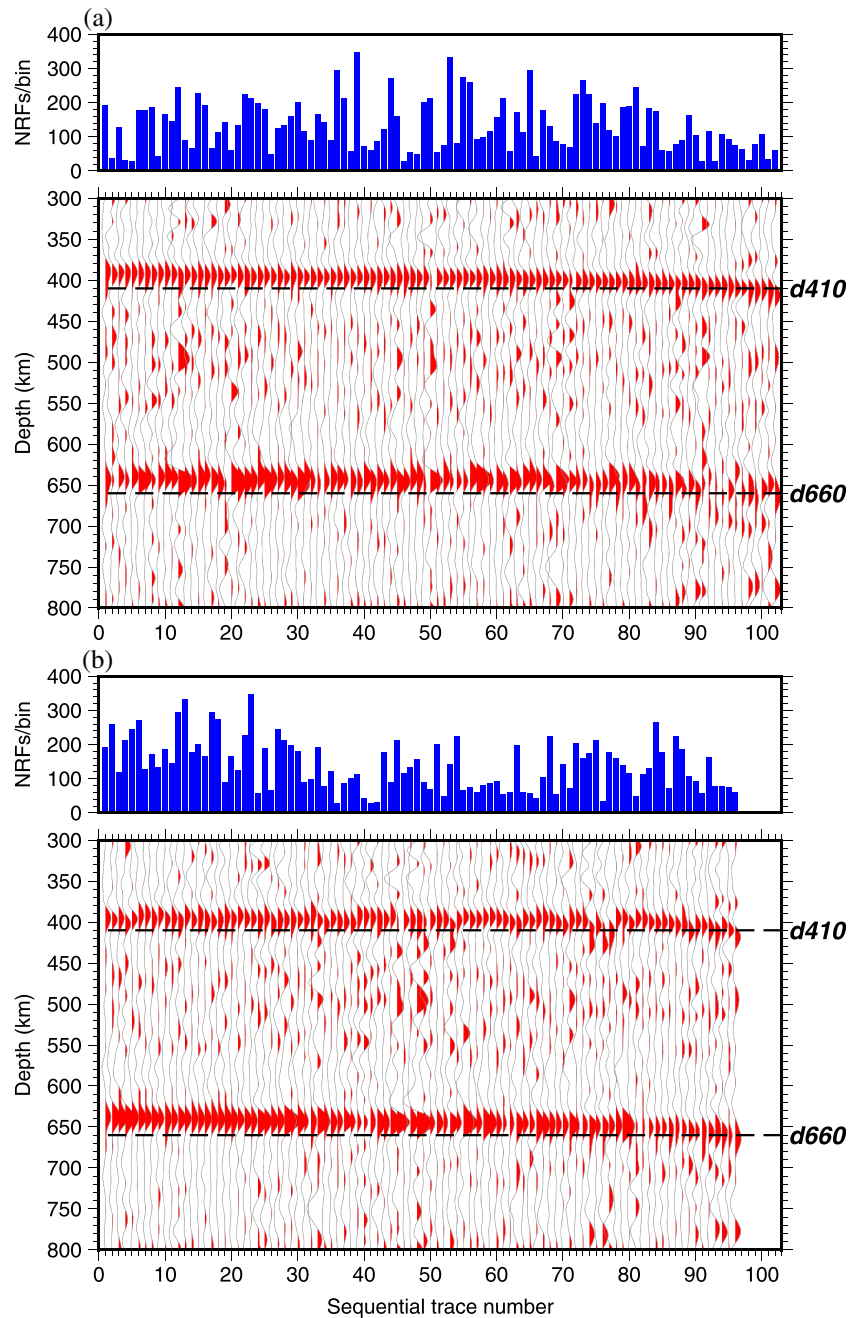
Figure 5. Binned RFs sorted according to the increasing apparent depth of (a) the d410 and (b) the d660. Blue bars in the top panel of (a) and (b) indicate the number of RFs used for moveout correction and stacking for each corresponding bin in the lower panel.

of 400 ± 1 and 648 ± 1 km, respectively) are approximately elevated by about 10 km with a mean MTZ thickness of 247 ± 3 km. The area with slight MTZ thinning south of the ORZ that was partially revealed in an earlier RF study (Yu, Liu, Moidaki, et al., 2015) has an NE-SW elongated shape (Figure 6), and the average MTZ discontinuity depths and thickness in this area are 398 ± 3, 639 ± 2, and 240 ± 3 km, respectively. This area with slightly thinned MTZ is mostly occupied by the Ghanzi ridge, which is interpreted as the initial updoming associated with the southward extension of the ORZ (e.g., Gumbricht et al., 2001). A few other isolated areas with smaller magnitudes of MTZ thinning are also revealed (Figure 6d). The MTZ beneath most of the southern Rehoboth Province, which was not covered by
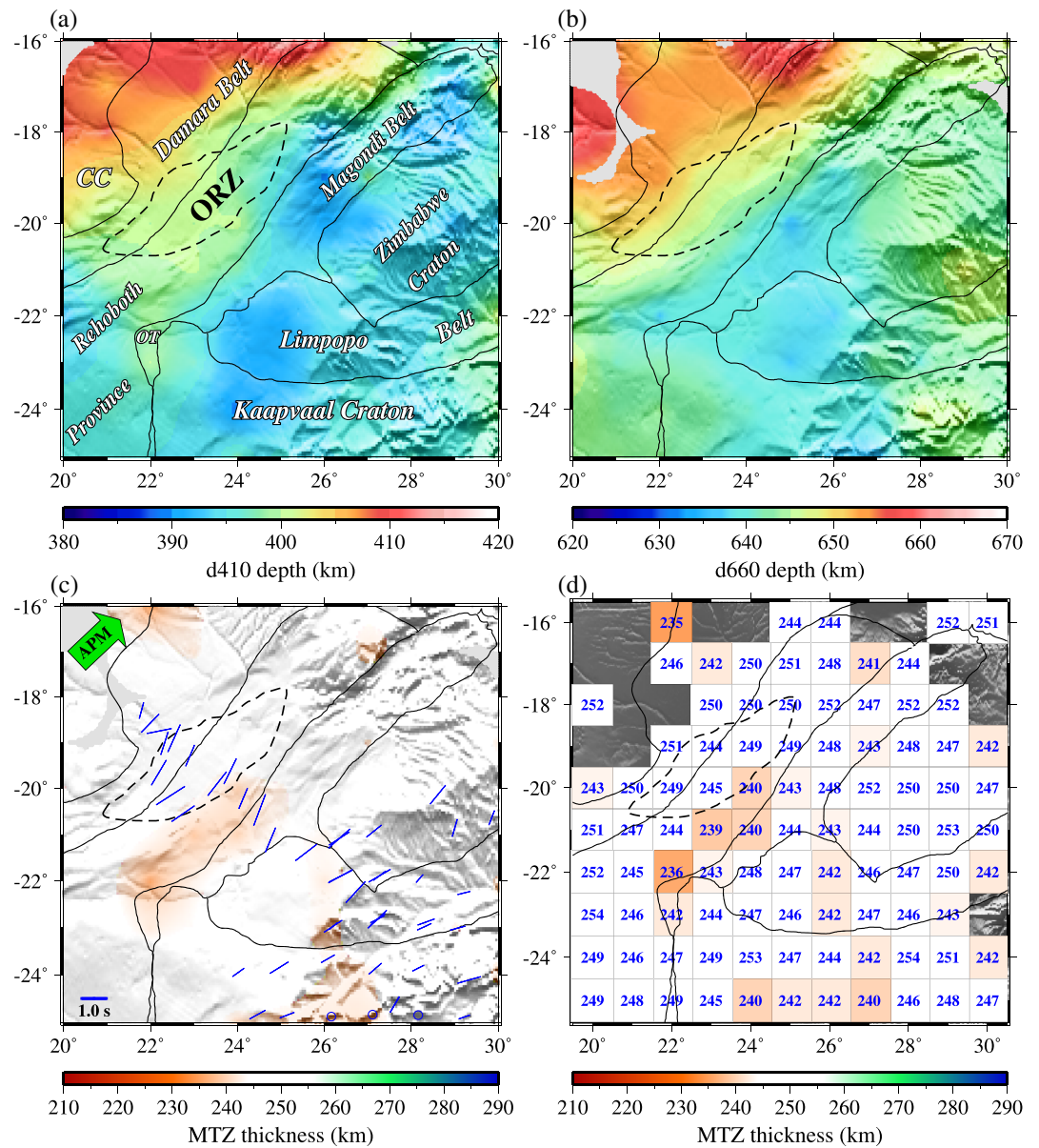
Figure 6. (a) Spatial distribution of the resulting apparent depths of the d410. (b) Same as (a) but for the d660. (c) Smoothed contour of MTZ thickness. Green arrow represents the absolute plate motion (APM) direction according to the NNR-MORVEL56 model (Argus et al., 2011). Blue bars indicate station-averaged shear wave splitting measurements from previous studies (Silver et al., 2001; Yu, Gao, et al., 2015). (d) Same as (c) but for the discrete value of MTZ thickness at each bin.

previous studies, shows a normal thickness (249 ± 3 km) and apparently shallower-than-normal d410 (395 ± 1 km) and d660 (643 ± 2 km).

3.2. Estimated Lithospheric Thickness and Comparison With Previous Studies

In spite of the fact that a number of parameters have been assumed when estimating the lithospheric structure based on the apparent depths of the d410, the resulting lithospheric thickness (ranging from 51 to 347 km with an average of 210 ± 64 km) is generally consistent with what was obtained from other geophysical investigations especially with the seismologically determined measurements (e.g., Eaton et al., 2009). The spatial distribution of the estimated thickness closely follows the tectonic boundaries observed at the surface (Figure 8) where cratonic and Proterozoic orogenic areas are characterized as possessing relatively
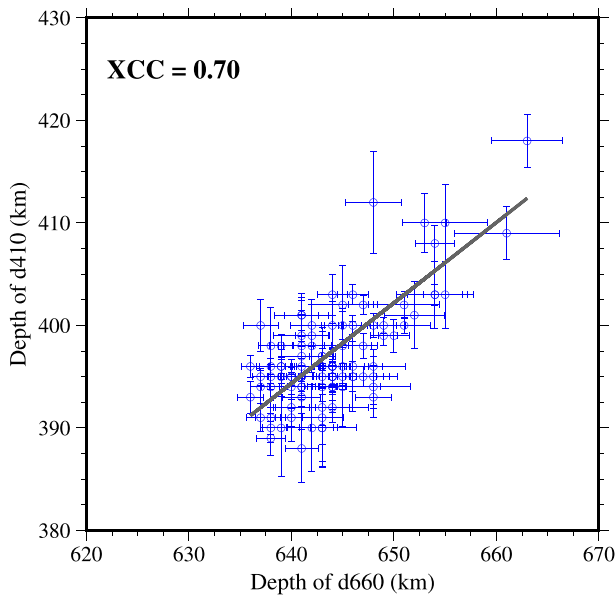
Figure 7. Cross correlation between the resulting apparent depths of the d410 and d660. XCC = cross-correlation coefficient.

thick and thin lithosphere, respectively. The XCCs between the estimated lithospheric thickness and those from large-scale models of Conrad and Lithgow-Bertelloni (2006) and Pasyanos et al. (2014) are determined to be 0.7 and 0.51, respectively (Figure S4).

Thick lithosphere beneath the Kalahari Craton is revealed with an average thickness of 242 ± 39 km, which is comparable to values of about 220 km from magnetotelluric (MT) inversions (e.g., Evans et al., 2011; Miensopust et al., 2011; Muller et al., 2009) and ~200 km or greater determined from a recent surface wave tomography study (Fadel et al., 2020). Both the southern Rehoboth Province (241 ± 35 km) and the Magondi Belt (251 ± 41 km) have a lithospheric thickness that is comparable with that of the Kalahari Craton, an observation that is consistent with the suggestion that both areas represent the westward extension of cratonic lithosphere based on craton-like high-velocity anomalies (Ortiz et al., 2019) and similar electrical structure (Muller et al., 2009). A recent surface wave tomography investigation (Fadel et al., 2020) attributes the thick lithosphere beneath the southern Rehoboth Province to the presence of the Maltahohe microcraton (Begg et al., 2009), which is further supported by a crustal thickness of 42 km that is similar to the other cratonic regions in Botswana (Fadel et al., 2018).

The derived lithospheric thickness beneath the southern edge of the Congo Craton (111 ± 40 km), however, is much smaller than that obtained based on MT studies (Khoza et al., 2013). The Congo Craton is imaged to extend into Botswana and possess a resistive thick (about 250 km) and cold lithosphere (Khoza et al., 2013), which is consistent with results from seismic tomographic studies (Figure 8; Fadel et al., 2020; Ortiz et al., 2019; Yu et al., 2017). One of the possible causes of this discrepancy is the existence of relatively significant low-velocity anomalies in the upper mantle (Figure 8), which is also revealed by the recent surface wave tomography (Fadel et al., 2020) and would reduce the resulting lithospheric thickness. Although there is also a slight low-velocity anomaly beneath the ORZ (Figure 8), the mean thickness of the lithosphere beneath the ORZ (189 ± 15 km) is comparable to the value of about 160 km or so reported from inversion of MT (Khoza et al., 2013; Muller et al., 2009) and surface wave data (Fadel et al., 2020).

4. Discussion

4.1. Lack of Widespread Thermal Upwelling Through the MTZ Beneath the ORZ

The resulting nearly normal MTZ thickness revealed beneath the ORZ is inconsistent with the existence of one or more active hot mantle upwellings beneath the incipient continental rift, an observation that is also in agreement with results from other geophysical investigations (e.g., Fadel et al., 2020; Khoza et al., 2013; Ortiz et al., 2019; Yu et al., 2017; Yu, Liu, Moidaki, et al., 2015). For instance, strain localization during the initiation of the ORZ is proposed to be promoted by fluid-assisted lithospheric weakening without asthenospheric involvement based on the shallow Curie point depth values and high heat flow along major rift-related border faults and the Proterozoic orogenic bounders (Leseane et al., 2015). The recent crustal and upper mantle shear wave velocity model of Botswana from Rayleigh wave inversion (Fadel et al., 2020) indicates that fluids or melt in the lower crust and uppermost mantle beneath the ORZ is connected to the continuation of the southwestern branch of the EARS. A lack of elevated mantle conductivity has been revealed from inversion of MT data (Khoza et al., 2013), and tomography studies (Ortiz et al., 2019; Yu et al., 2017) have suggested that a localized low-velocity anomaly is constrained in the upper asthenosphere beneath the ORZ without reaching the MTZ. In addition, the existence of a hot mantle upwelling would be expected to generate complex or radial patterns of azimuthal anisotropy, which is inconsistent with the uniformly absolute plate motion (APM)-parallel fast orientations (Figure 6) beneath the ORZ and its surrounding areas (Yu, Gao, et al., 2015). The lack of a large-scale thermal anomaly in the MTZ usually associated with a mantle plume is also suggested beneath mature rift zones such as the Rio Grande (Wilson et al., 2005) and Baikal (Liu & Gao, 2006) rifts.
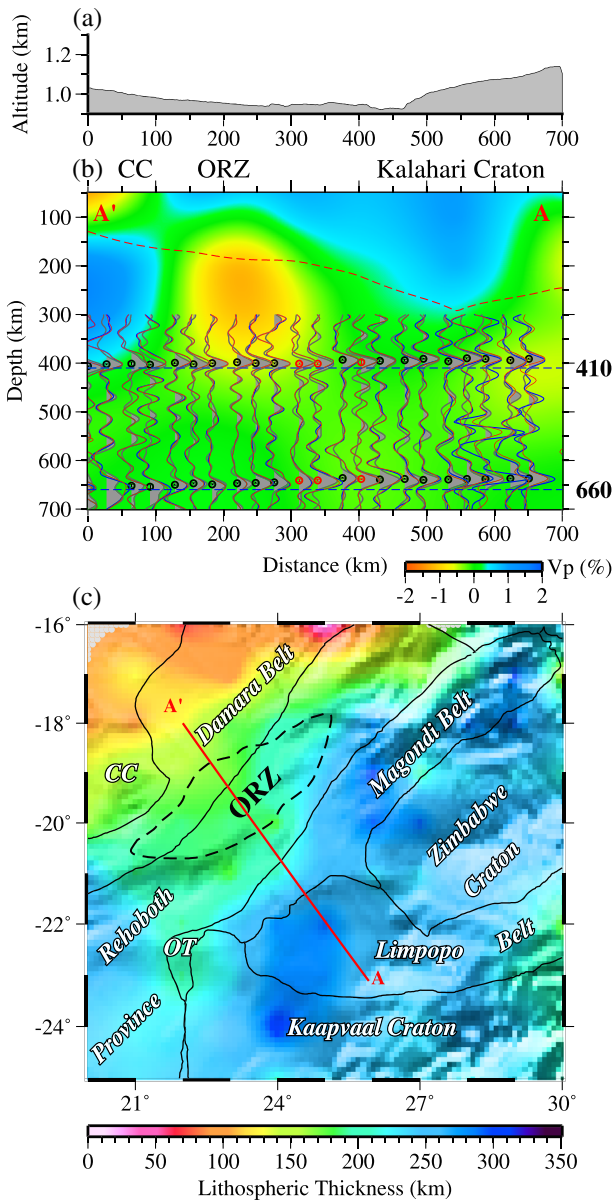
Figure 8. Vertical cross section of resulting depth series and map view of estimated lithospheric thickness derived from the d410 depth. (a) Surface topography along Profile A ′ A in (c). (b) Depth series and estimated lithospheric thickness (red dashed lines). The background image shows the *P* wave tomography model of Yu et al. (2017). Black and red circles represent the determined apparent depths of the MTZ discontinuities, among which the red ones indicate those with MTZ thickness less than 240 km, and the black ones are for those greater than or equal to 240 km. Gray, red, and blue traces indicate depth series from the current study, Yu, Liu, Moidaki, et al. (2015), and Sun et al. (2018), respectively. The blue dashed lines represent the IASP91 depths of the d410 and d660. (c) Spatial distribution of estimated lithospheric thickness derived from the resulting apparent depth of the d410.

4.2. Possible Thermal Upwellings Beneath Isolated Areas

An area of thinner-than-normal MTZ was observed near the south side of the ORZ by Yu, Liu, Moidaki, et al. (2015) using the SAFARI data alone. Because this area is located near the edge of the area sparsely sampled by the RFs, its spatial extent and geometry could not be determined. Results using the expanded data set suggest that the area has a NE-SW elongated shape, with a maximum amount of MTZ thinning of 14 km located at (22°E, 22°S) (Figure 6d), which corresponds to a positive thermal anomaly of 120°C if Clapeyron slopes of 2.9 MPa/K (an average value from Bina & Helffrich, 1994) for the d410 and −1.3 MPa/K (determined by Fei et al., 2004) for the d660 are used. MTZ thinning is also suggested beneath the Main Ethiopian and Kenyan rifts and has been interpreted to be possibly related to the African Superplume (Cornwell et al., 2011; Huerta et al., 2009), but such an interpretation has recently been challenged (Sun et al., 2017). Although the magnitude of the thermal anomaly is comparable with what has been proposed for a moderate mantle plume (Farnetani & Richards, 1994), the observations cannot adequately support a mantle plume originated from the lower mantle and extends to the surface, for a number of reasons. First, the area with thinner-than-normal MTZ has an elongated rather than the typical circular shape that is expected for the horizontal cross section of a mantle plume as observed beneath Iceland and Hawaii. Second, if the temperature anomaly extends to the surface from the d410, a mean V_P anomaly of about −1.0% and a V_S anomaly of about −1.8% in the upper mantle are expected. Such negative velocity anomalies are not observed by any of the previous seismic tomographic studies (e.g., Ortiz et al., 2019; Yu et al., 2017). On the contrary, the shallower-than-normal apparent depths in virtually all the study area indicate the existence of higher- rather than lower-than-normal velocity anomalies in the upper mantle. Third, as demonstrated by the depth series for the bin with the thinnest MTZ (the third trace from the left-hand side in Figure 4g), the MTZ thinning is mostly caused by an apparent deepening of the d410 rather than the uplift of the d660, which is further confirmed by the velocity-corrected depths (Figures S2 and S3). The thermal anomaly is more likely located in the upper MTZ than being associated with a lower mantle thermal anomaly traversing the whole MTZ.

The causes of the thinned MTZ beneath this and a few other smaller areas are unclear. Numerical modeling (Korenaga, 2004) indicates that small-scale mantle upwelling can be triggered by lateral heterogeneities at the base of the MTZ. Although such heterogeneities have not been detected, a recent study on the western Gondwana Craton (Hu et al., 2018) that includes the study area suggests that materials of neutrally buoyant lithosphere piles are possibly accumulated above the lower mantle due to plume-triggered delamination of cratonic roots during the late Cretaceous and early Cenozoic periods. These materials may trigger minor thermal upwelling, a mechanism proposed to explain the topography of MTZ discontinuities beneath southern California (Yu et al., 2020).

4.3. Absence of Thermal Effects From the African LLSVP and Cratonic Roots

Most of the southern African plate and its neighboring oceanic areas are imaged to possess a large-scale low-velocity anomaly in the lower mantle (the African LLSVP, e.g., Lithgow-Bertelloni & Silver, 1998; Ritsema et al., 2011). Our widespread observations of normal MTZ thickness suggest that the LLSVP has limited

effects on the thermal structure of the MTZ beneath our study region, a conclusion that is consistent with previous MTZ investigations (Gao et al., 2002; Julià & Nyblade, 2013; Niu et al., 2004; Sun et al., 2018; Yu, Liu, Moidaki, et al., 2015). Azimuthal anisotropy beneath southern Africa (Figure 6) is found to have systematically APM-parallel NE-SW fast orientations (e.g., Reed et al., 2017; Silver et al., 2001; Yu, Gao, et al., 2015), and the optimal depth of its center is determined to range between 240 and 280 km, which is proposed to be due to the simple shear between the lithosphere and asthenosphere driven by the long-term plate motions without the involvement of the African LLSVP (Yu, Gao, et al., 2015). A recent body wave tomography study of the top 900 km of the Earth beneath southern Africa shows a lack of widespread low-velocity anomalies (Ortiz et al., 2019). Thus, the high-temperature African LLSVP is most likely constrained in the lower mantle and has indiscernible influences on the MTZ structure of our study area. However, results from this study are not inconsistent with the suggestion that mantle upwelling from the African LLSVP may tilt northward outside of our study area into southern Zambia where low-velocity anomalies are revealed to extend into the MTZ (Ortiz et al., 2019).

The thick lithosphere beneath the Kalahari and Congo cratons is commonly revealed from surface-wave (e.g., Chevrot & Zhao, 2007; Fadel et al., 2020; Li & Burke, 2006) and body wave tomography (James et al., 2001; Ortiz et al., 2019; Youssof et al., 2015; Yu et al., 2017), RF (Wittlinger & Farra, 2007), and MT studies (e.g., Evans et al., 2011; Khoza et al., 2013; Miensopust et al., 2011; Muller et al., 2009). Most body wave tomography investigations report a much thicker lithosphere (Figure 8) beneath the Kaapvaal and Zimbabwe cratons extending to depths of at least 250 km and locally reaches 300–350 km (e.g., James et al., 2001; Youssof et al., 2015), which is comparable to the average value of 300 km from inversion of RFs (Wittlinger & Farra, 2007). A cold and water-enriched MTZ beneath the Kalahari Craton was proposed based on a thickened MTZ by as much as 20 km, which was interpreted as due to the extension of the thick cratonic keels (Blum & Shen, 2004). The absence of MTZ thickening revealed in this and most other MTZ studies indicates that the cratonic roots beneath our study area are well constrained in the upper mantle and have insignificant influence on the thermal structure of the MTZ.

5. Conclusions

By combining broadband seismic data used in a previous MTZ discontinuity study (Yu, Liu, Moidaki, et al., 2015) and data recorded in a greater area in Botswana, we systematically map the topography of the d410 and d660 beneath the ORZ and its surrounding regions. The greatly improved spatial coverage and the increase in the number of RFs in many of the bins as a result of the addition of the new stations led to robust constraints on the thermal structure of the MTZ and its geodynamic implications. Normal MTZ thicknesses are found beneath the incipient ORZ, suggesting the absence of widespread thermal upwelling from the lower mantle. The cold cratonic roots and the high temperature possibly associated with the southern African LLSVP have no observable effects on the temperature distribution in the MTZ. A strong positive cross correlation between the apparent depths of the d410 and d660 suggests that the apparent undulations of the d410 and d660 depths obtained using the 1-D IASP91 Earth model are mostly caused by lateral velocity variations in the upper mantle, which may be largely attributable to changes in lithospheric thickness. Higher-than-normal temperature in the upper MTZ beneath a NE-SW elongated area of slight MTZ thinning south of the ORZ and beneath a few other smaller areas may reflect thermal upwelling induced by lithospheric delamination that was recently proposed to have occurred in late Mesozoic and early Cenozoic.

Data Availability Statement

References

Ammon, C. J. (1991). The isolation of receiver effects from teleseismic *P* waveforms. *Bulletin of the Seismological Society of America*, *81*(6), 2504–2510.

Argus, D. F., Gordon, R. G., & DeMets, C. (2011). Geologically current motion of 56 plates relative to the no-net-rotation reference frame. *Geochemistry, Geophysics, Geosystems*, *12*, Q11001. https://doi.org/10.1029/2011GC003751

Begg, G. C., Griffin, W. L., Natapov, L. M., O'Reilly, S. Y., Grand, S. P., O'Neill, C. J., et al. (2009). The lithospheric architecture of Africa: Seismic tomography, mantle petrology, and tectonic evolution. *Geosphere*, *5*(1), 23–50. https://doi.org/10.1130/GES00179.1

Bina, C. R., & Helffrich, G. (1994). Phase transition Clapeyron slopes and transition zone seismic discontinuity topography. *Journal of Geophysical Research*, *99*(B8), 15,853–15,860. https://doi.org/10.1029/94JB00462

Blum, J., & Shen, Y. (2004). Thermal, hydrous, and mechanical states of the mantle transition zone beneath southern Africa. *Earth and Planetary Science Letters*, *217*(3–4), 367–378. https://doi.org/10.1016/S0012-821X(03)00628-9

Chevrot, S., & Zhao, L. (2007). Multiscale finite-frequency Rayleigh wave tomography of the Kaapvaal craton. *Geophysical Journal International*, *169*(1), 201–215. https://doi.org/10.1111/j.1365-246X.2006.03289.x

Conrad, C. P., & Lithgow-Bertelloni, C. (2006). Influence of continental roots and asthenosphere on plate-mantle coupling. *Geophysical Research Letters*, *33*, L05312. https://doi.org/10.1029/2005GL025621

Cornwell, D. G., Hetényi, G., & Blanchard, T. D. (2011). Mantle transition zone variations beneath the Ethiopian Rift and Afar: Chemical heterogeneity within a hot mantle? *Geophysical Research Letters*, *38*, L16308. https://doi.org/10.1029/2011GL047575

De Wit, M. J., de Ronde, C. E., Tredoux, M., Roering, C., Hart, R. J., Armstrong, R. A., et al. (1992). Formation of an Archaean continent. *Nature*, *357*(6379), 553–562. https://doi.org/10.1038/357553a0

Eaton, D. W., Darbyshire, F., Evans, R. L., Grütter, H., Jones, A. G., & Yuan, X. (2009). The elusive lithosphere-asthenosphere boundary (LAB) beneath cratons. *Lithos*, *109*(1–2), 1–22. https://doi.org/10.1016/j.lithos.2008.05.009

Efron, B., & Tibshirani, R. (1986). Bootstrap methods for standard errors, confidence intervals, and other measures of statistical accuracy. *Statistical Science*, *1*(1), 54–75. https://doi.org/10.1214/ss/1177013815

Evans, R. L., Jones, A. G., Garcia, X., Muller, M., Hamilton, M., Evans, S., et al. (2011). Electrical lithosphere beneath the Kaapvaal craton, southern Africa. *Journal of Geophysical Research*, *116*, B04105. https://doi.org/10.1029/2010JB007883

Fadel, I., Paulssen, H., van der Meijde, M., Kwadiba, M., Ntibinyane, O., Nyblade, A., & Durrheim, R. (2020). Crustal and upper mantle shear wave velocity structure of Botswana: The 3 April 2017 central Botswana earthquake linked to the East African Rift System. *Geophysical Research Letters*, *47*, e2019GL085598. https://doi.org/10.1029/2019GL085598

Fadel, I., van der Meijde, M., & Paulssen, H. (2018). Crustal structure and dynamics of Botswana. *Journal of Geophysical Research: Solid Earth*, *123*, 10,659–10,671. https://doi.org/10.1029/2018JB016190

Farnetani, C. G., & Richards, M. A. (1994). Numerical investigations of the mantle plume initiation model for flood basalt events. *Journal of Geophysical Research*, *99*(B7), 13,813–13,833. https://doi.org/10.1029/94JB00649

Fei, Y., Van Orman, J., Li, J., Van Westrenen, W., Sanloup, C., Minarik, W., et al. (2004). Experimentally determined postspinel transformation boundary in Mg_2SiO_4 using MgO as an internal pressure standard and its geophysical implications. *Journal of Geophysical Research*, *109*, B02305. https://doi.org/10.1029/2003JB002562

Fishwick, S., & Bastow, I. D. (2011). Towards a better understanding of African topography: A review of passive-source seismic studies of the African crust and upper mantle. *Geological Society, London, Special Publications*, *357*(1), 343–371. https://doi.org/10.1144/SP357.19

Foulger, G. R., Panza, G. F., Artemieva, I. M., Bastow, I. D., Cammarano, F., Evans, J. R., et al. (2013). Caveats on tomographic images. *Terra Nova*, *25*(4), 259–281. https://doi.org/10.1111/ter.12041

Gao, S. S., & Liu, K. H. (2014a). Imaging mantle discontinuities using multiply-reflected *P*-to-*S* conversions. *Earth and Planetary Science Letters*, *402*, 99–106. https://doi.org/10.1016/j.epsl.2013.08.025

Gao, S. S., & Liu, K. H. (2014b). Mantle transition zone discontinuities beneath the contiguous United States. *Journal of Geophysical Research: Solid Earth*, *119*, 6452–6468. https://doi.org/10.1002/2014JB011253

Gao, S. S., Liu, K. H., Reed, C. A., Yu, Y., Massinque, B., Mdala, H., et al. (2013). Seismic arrays to study African rift initiation. *Eos, Transactions American Geophysical Union*, *94*(24), 213–214. https://doi.org/10.1002/2013EO240002

Gao, S. S., Silver, P. G., Liu, K. H., & Kaapvaal Seismic Group (2002). Mantle discontinuities beneath southern Africa. *Geophysical Research Letters*, *29*(10), 129-1–129-4. https://doi.org/10.1029/2001GL013834

Gumbricht, T., McCarthy, T. S., & Merry, C. L. (2001). The topography of the Okavango Delta, Botswana, and its tectonic and sedimentological implications. *South African Journal of Geology*, *104*(3), 243–264. https://doi.org/10.2113/1040243

Gurnis, M., Mitrovica, J. X., Ritsema, J., & van Heijst, H. J. (2000). Constraining mantle density structure using geological evidence of surface uplift rates: The case of the African superplume. *Geochemistry, Geophysics, Geosystems*, *1*(7). https://doi.org/10.1029/1999GC000035

Hansen, S. E., Nyblade, A. A., & Benoit, M. H. (2012). Mantle structure beneath Africa and Arabia from adaptively parameterized *P*-wave tomography: Implications for the origin of Cenozoic Afro-Arabian tectonism. *Earth and Planetary Science Letters*, *319–320*, 23–34. https://doi.org/10.1016/j.epsl.2011.12.023

Hanson, R. E. (2003). Proterozoic geochronology and tectonic evolution of southern Africa. *Geological Society, London, Special Publications*, *206*(1), 427–463. https://doi.org/10.1144/GSL.SP.2003.206.01.20

Hirose, K. (2002). Phase transitions in pyrolitic mantle around 670-km depth: Implications for upwelling of plumes from the lower mantle. *Journal of Geophysical Research*, *107*(B4). https://doi.org/10.1029/2001JB000597

Hu, J., Liu, L., Faccenda, M., Zhou, Q., Fischer, K. M., Marshak, S., & Lundstrom, C. (2018). Modification of the Western Gondwana craton by plume–lithosphere interaction. *Nature Geoscience*, *11*(3), 203–210. https://doi.org/10.1038/s41561-018-0064-1

Huerta, A. D., Nyblade, A. A., & Reusch, A. M. (2009). Mantle transition zone structure beneath Kenya and Tanzania: More evidence for a deep-seated thermal upwelling in the mantle. *Geophysical Journal International*, *177*(3), 1249–1255. https://doi.org/10.1111/j.1365-246X.2009.04092.x

James, D. E., Fouch, M. J., VanDecar, J. C., Van Der Lee, S., & Kaapvaal Seismic Group (2001). Tectospheric structure beneath southern Africa. *Geophysical Research Letters*, *28*(13), 2485–2488. https://doi.org/10.1029/2000GL012578

Julià, J., & Nyblade, A. A. (2013). Probing the upper mantle transition zone under Africa with P520s conversions: Implications for temperature and composition. *Earth and Planetary Science Letters*, *368*, 151–162. https://doi.org/10.1016/j.epsl.2013.02.021

Kennett, B. L. N., & Engdahl, E. R. (1991). Traveltimes for global earthquake location and phase identification. *Geophysical Journal International*, *105*(2), 429–465. https://doi.org/10.1111/j.1365-246X.1991.tb06724.x

Khoza, T. D., Jones, A. G., Muller, M. R., Evans, R. L., Miensopust, M. P., & Webb, S. J. (2013). Lithospheric structure of an Archean craton and adjacent mobile belt revealed from 2-D and 3-D inversion of magnetotelluric data: Example from southern Congo craton in northern Namibia. *Journal of Geophysical Research: Solid Earth*, *118*, 4378–4397. https://doi.org/10.1002/jgrb.50258

King, S. D., & Anderson, D. L. (1998). Edge-driven convection. *Earth and Planetary Science Letters*, *160*(3–4), 289–296. https://doi.org/10.1016/S0012-821X(98)00089-2

Korenaga, J. (2004). Mantle mixing and continental breakup magmatism. *Earth and Planetary Science Letters*, *218*(3–4), 463–473. https://doi.org/10.1016/S0012-821X(03)00674-5

Leseane, K., Atekwana, E. A., Mickus, K. L., Abdelsalam, M. G., Shemang, E. M., & Atekwana, E. A. (2015). Thermal perturbations beneath the incipient Okavango Rift Zone, northwest Botswana. *Journal of Geophysical Research: Solid Earth*, *120*, 1210–1228. https://doi.org/10.1002/2014JB011029

Li, A., & Burke, K. (2006). Upper mantle structure of southern Africa from Rayleigh wave tomography. *Journal of Geophysical Research Solid Earth*, *111*, B10303. https://doi.org/10.1029/2006JB004321

Litasov, K. D., Ohtani, E., Sano, A., Suzuki, A., & Funakoshi, K. (2005). Wet subduction versus cold subduction. *Geophysical Research Letters*, *32*, L13312. https://doi.org/10.1029/2005GL022921

Lithgow-Bertelloni, C., & Silver, P. G. (1998). Dynamic topography, plate driving forces and the African superswell. *Nature*, *395*(6699), 269–272. https://doi.org/10.1038/26212

Liu, K. H., & Gao, S. S. (2006). Mantle transition zone discontinuities beneath the Baikal rift and adjacent areas. *Journal of Geophysical Research*, *111*, B11301. https://doi.org/10.1029/2005JB004099

Liu, K. H., & Gao, S. S. (2010). Spatial variations of crustal characteristics beneath the Hoggar swell, Algeria, revealed by systematic analyses of receiver functions from a single seismic station. *Geochemistry, Geophysics, Geosystems*, *11*, Q08011. https://doi.org/10.1029/2010GC003091

Lu, C., Grand, S. P., Lai, H., & Garnero, E. J. (2019). TX2019slab: A new *P* and *S* tomography model incorporating subducting slabs. *Journal of Geophysical Research: Solid Earth*, *124*, 11,549–11,567. https://doi.org/10.1029/2019JB017448

Miensopust, M. P., Jones, A. G., Muller, M. R., Garcia, X., & Evans, R. L. (2011). Lithospheric structures and Precambrian terrane boundaries in northeastern Botswana revealed through magnetotelluric profiling as part of the Southern African Magnetotelluric Experiment. *Journal of Geophysical Research*, *116*, B02401. https://doi.org/10.1029/2010JB007740

Modisi, M. P., Atekwana, E. A., Kampunzu, A. B., & Ngwisanyi, T. H. (2000). Rift kinematics during the incipient stages of continental extension: Evidence from the nascent Okavango rift basin, northwest Botswana. *Geology*, *28*(10), 939–942. https://doi.org/10.1130/0091-7613(2000)28<939:RKDTIS>2.0.CO;2

Mohamed, A. A., Gao, S. S., Elsheikh, A. A., Liu, K. H., Yu, Y., & Fat-Helbary, R. E. (2014). Seismic imaging of mantle transition zone discontinuities beneath the northern Red Sea and adjacent areas. *Geophysical Journal International*, *199*(2), 648–657. https://doi.org/10.1093/gji/ggu284

Mulibo, G. D., & Nyblade, A. A. (2013). The *P* and *S* wave velocity structure of the mantle beneath eastern Africa and the African superplume anomaly. *Geochemistry, Geophysics, Geosystems*, *14*, 2696–2715. https://doi.org/10.1002/ggge.20150

Muller, M. R., Jones, A. G., Evans, R. L., Grütter, H. S., Hatton, C., Garcia, X., et al. (2009). Lithospheric structure, evolution and diamond prospectivity of the Rehoboth Terrane and western Kaapvaal Craton, southern Africa: Constraints from broadband magnetotellurics. *Lithos*, *112*, 93–105. https://doi.org/10.1016/j.lithos.2009.06.023

Niu, F., Levander, A., Cooper, C. M., Lee, C. T. A., Lenardic, A., & James, D. E. (2004). Seismic constraints on the depth and composition of the mantle keel beneath the Kaapvaal craton. *Earth and Planetary Science Letters*, *224*(3–4), 337–346. https://doi.org/10.1016/j.epsl.2004.05.011

Ortiz, K., Nyblade, A., van der Meijde, M., Paulssen, H., Kwadiba, M., Ntibinyane, O., et al. (2019). Upper mantle *P*- and *S*-wave velocity structure of the Kalahari Craton and surrounding Proterozoic terranes, southern Africa. *Geophysical Research Letters*, *46*, 9509–9518. https://doi.org/10.1029/2019GL084053

Pasyanos, M. E., Masters, T. G., Laske, G., & Ma, Z. (2014). LITHO1.0: An updated crust and lithospheric model of the Earth. *Journal of Geophysical Research: Solid Earth*, *119*, 2153–2173. https://doi.org/10.1002/2013JB010626

Reed, C. A., Liu, K. H., Chindandali, P. R., Massingue, B., Mdala, H., Mutamina, D., et al. (2016). Passive rifting of thick lithosphere in the southern East African Rift: Evidence from mantle transition zone discontinuity topography. *Journal of Geophysical Research: Solid Earth*, *121*, 8068–8079. https://doi.org/10.1002/2016JB013131

Reed, C. A., Liu, K. H., Yu, Y., & Gao, S. S. (2017). Seismic anisotropy and mantle dynamics beneath the Malawi Rift Zone, East Africa. *Tectonics*, *36*, 1338–1351. https://doi.org/10.1002/2017TC004519

Reeves, C. V. (1972). Rifting in the Kalahari? *Nature*, *237*(5350), 95–96. https://doi.org/10.1038/237095a0

Ringwood, A. E. (1975). *Composition and petrology of the Earth's mantle* (1st ed., Vol. 672). New York: McGraw-Hill.

Ritsema, J., Deuss, A. A., Van Heijst, H. J., & Woodhouse, J. H. (2011). S40RTS: A degree-40 shear-velocity model for the mantle from new Rayleigh wave dispersion, teleseismic traveltime and normal-mode splitting function measurements. *Geophysical Journal International*, *184*(3), 1223–1236. https://doi.org/10.1111/j.1365-246X.2010.04884.x

Rychert, C. A., Hammond, J. O., Harmon, N., Kendall, J. M., Keir, D., Ebinger, C., et al. (2012). Volcanism in the Afar Rift sustained by decompression melting with minimal plume influence. *Nature Geoscience*, *5*(6), 406–409. https://doi.org/10.1038/NGEO1455

Rychert, C. A., & Shearer, P. M. (2009). A global view of the lithosphere-asthenosphere boundary. *Science*, *324*(5926), 495–498. https://doi.org/10.1126/science.1169754

Sengör, A. C., & Burke, K. (1978). Relative timing of rifting and volcanism on Earth and its tectonic implications. *Geophysical Research Letters*, *5*(6), 419–421. https://doi.org/10.1029/GL005i006p00419

Silver, P. G., Gao, S. S., Liu, K. H., & Kaapvaal Seismic Group (2001). Mantle deformation beneath southern Africa. *Geophysical Research Letters*, *28*(13), 2493–2496. https://doi.org/10.1029/2000GL012696

Stamps, D. S., Iaffaldano, G., & Calais, E. (2015). Role of mantle flow in Nubia-Somalia plate divergence. *Geophysical Research Letters*, *42*, 290–296. https://doi.org/10.1002/2014GL062515

Sun, M., Fu, X., Liu, K. H., & Gao, S. S. (2018). Absence of thermal influence from the African Superswell and cratonic keels on the mantle transition zone beneath southern Africa: Evidence from receiver function imaging. *Earth and Planetary Science Letters*, *503*, 108–117. https://doi.org/10.1016/j.epsl.2018.09.012

Sun, M., Liu, K. H., Fu, X., & Gao, S. S. (2017). Receiver function imaging of mantle transition zone discontinuities beneath the Tanzania Craton and adjacent segments of the East African Rift System. *Geophysical Research Letters*, *44*, 12,116–12,124. https://doi.org/10.1002/2017GL075485

Wilson, D., Aster, R., Ni, J., Grand, S., West, M., Gao, W., et al. (2005). Imaging the seismic structure of the crust and upper mantle beneath the Great Plains, Rio Grande Rift, and Colorado Plateau using receiver functions. *Journal of Geophysical Research*, *110*, B05306. https://doi.org/10.1029/2004JB003492

Wittlinger, G., & Farra, V. (2007). Converted waves reveal a thick and layered tectosphere beneath the Kalahari super-craton. *Earth and Planetary Science Letters*, *254*(3–4), 404–415. https://doi.org/10.1016/j.epsl.2006.11.048

Youssof, M., Thybo, H., Artemieva, I. M., & Levander, A. (2015). Upper mantle structure beneath southern African cratons from seismic finite-frequency *P*- and *S*-body wave tomography. *Earth and Planetary Science Letters*, *420*, 174–186. https://doi.org/10.1016/j.epsl.2015.01.034

Yu, Y., Gao, S. S., Liu, K. H., & Zhao, D. (2020). Foundered lithospheric segments dropped into the mantle transition zone beneath southern California, USA. *Geology*, *48*. https://doi.org/10.1130/G46889.1

Yu, Y., Gao, S. S., Moidaki, M., Reed, C. A., & Liu, K. H. (2015). Seismic anisotropy beneath the incipient Okavango rift: Implications for rifting initiation. *Earth and Planetary Science Letters*, *430*, 1–8. https://doi.org/10.1016/j.epsl.2015.08.009

Yu, Y., Liu, K. H., Huang, Z., Zhao, D., Reed, C. A., Moidaki, M., et al. (2017). Mantle structure beneath the incipient Okavango rift zone in southern Africa. *Geosphere*, *13*(1), 102–111. https://doi.org/10.1130/GES01331.1

Yu, Y., Liu, K. H., Moidaki, M., Reed, C. A., & Gao, S. S. (2015). No thermal anomalies in the mantle transition zone beneath an incipient continental rift: Evidence from the first receiver function study across the Okavango Rift Zone, Botswana. *Geophysical Journal International*, *202*(2), 1407–1418. https://doi.org/10.1093/gji/ggv229

Yu, Y., Liu, K. H., Reed, C. A., Moidaki, M., Mickus, K., Atekwana, E. A., & Gao, S. S. (2015). A joint receiver function and gravity study of crustal structure beneath the incipient Okavango Rift, Botswana. *Geophysical Research Letters*, *42*, 8398–8405. https://doi.org/10.1002/2015GL065811